

# **Discontinuity in equilibrium wave–current ripple size and shape caused by a winnowing threshold in cohesive sand–clay beds**

Xuxu Wu<sup>1</sup>, Roberto Fernández<sup>1</sup>, Jaco H. Baas<sup>2</sup>, Jonathan Malarkey<sup>1,2</sup>, Daniel R. Parsons<sup>1</sup>

<sup>1</sup>Energy and Environment Institute, University of Hull, Hull, HU6 7RX, England, UK

<sup>2</sup>School of Ocean Sciences, Bangor University, Menai Bridge, LL59 5AB, Wales, U.K.

Email addresses:

[X.Wu@hull.ac.uk](mailto:X.Wu@hull.ac.uk)

[R.Fernandez@hull.ac.uk](mailto:R.Fernandez@hull.ac.uk)

[J.Baas@bangor.ac.uk](mailto:J.Baas@bangor.ac.uk)

[J.Malarkey@bangor.ac.uk](mailto:J.Malarkey@bangor.ac.uk)

[D.Parsons@hull.ac.uk](mailto:D.Parsons@hull.ac.uk)

Twitter:

@stickyripple

@icemeanders

@making\_ripples

NA

@bedform

This is a non-peer reviewed preprint submitted to EarthArXiv. The manuscript has been submitted to the Journal of Geophysical Research: Earth Surface and is currently under consideration. Feel free to contact any of the authors with queries or to offer constructive feedback.

# Discontinuity in equilibrium wave–current ripple size and shape caused by a winnowing threshold in cohesive sand–clay beds

Xuxu Wu<sup>1</sup>, Roberto Fernández<sup>1</sup>, Jaco H. Baas<sup>2</sup>, Jonathan Malarkey<sup>1,2</sup>, Daniel R. Parsons<sup>1</sup>

<sup>1</sup>Energy and Environment Institute, University of Hull, Hull, HU6 7RX, England, UK

<sup>2</sup>School of Ocean Sciences, Bangor University, Menai Bridge, LL59 5AB, Wales, U.K.

## Key Points

- Ripple growth rates decrease with increasing initial bed clay content in sand-clay substrates under combined, wave-current, flows.
- Large ripples, comparable to clean-sand ones, can form below a clay content threshold, due to efficient winnowing and ‘deep cleaning’ of bed-clay.
- Small, flat ripples prevail when the clay content is above the threshold and strong bed cohesion prevents ripple growth.

## Abstract

Sediments composed of mixed cohesive clay and non-cohesive sand are widespread in a range of aquatic environments. The dynamics of ripples in mixed sand–clay substrates have been studied under pure current and pure wave conditions. However, the effect of cohesive clay on ripple development under combined currents and waves has not been examined, even though combined flows are common in estuaries, particularly during storms. Based on a series of large flume experiments on ripple development under combined flows, we identified a robust inverse relationship between initial bed clay content,  $C_0$ , and ripple growth rate. The experimental results also revealed two distinct types of equilibrium combined-flow ripples on mixed sand–clay beds: (a) large asymmetrical ripples with dimensions and plan geometries comparable to clean-sand counterparts for  $C_0 \leq 10.6\%$ ; and (b) small, flat ripples for  $C_0 > 11\%$ . The increase in bed cohesion contributed to this discontinuity, expressed most clearly in a sharp reduction in equilibrium ripple height, and thus a significant reduction in bed roughness, which implies

that the performance of existing ripple predictors can be improved by the incorporation of this physical cohesive effect. These improvements are particularly important for sediment transport and morphodynamic models in muddy estuarine environments. For  $C_0 \leq 10.6\%$ , strong clay winnowing efficiency under combined flows resulted in the formation of equilibrium clean-sand ripples and clay loss at depths far below the ripple base. In natural environments, this ‘deep cleaning’ of bed clay may cause a concurrent sudden release of a large amount of pollutants during storms, and lead to a sudden reduction in post-storm resistance to erosion of mixed sand–clay substrates.

## Plain Language Summary

Sticky-mud and sand are commonly found on estuary beds. Particularly during storms, the combined effect of waves and currents can erode the bed, creating small undulating shapes called ripples. For sand-only beds, the size of the ripples depends on the strength of the waves and currents that create them, and the size of the sand grains (fine sand is easier to erode than coarse sand). However, when sticky-mud is present, the growth of the ripples slows down. This study has identified that when waves and currents act at the same time: (1) Estuary beds with mixtures of sticky-mud and sand can form ripples with similar shape and size as clean-sand counterparts if the initial sticky-mud content is less than approximately 11%; (2) Estuary beds with an initial sticky-mud content higher than approximately 11% cannot be eroded and form very small ripples that are prevented from growing further due to the strength of the sticky-mud. The 11% threshold identified in this study is specific to the waves and currents tested, but the findings are generalizable and more research is required to identify the threshold under different wave-current combinations to better predict flow behaviours in muddy estuaries throughout the world.

## 1. Introduction

Ripples are primary sedimentary structures that are ubiquitous on the bed of estuaries and coastal seas. These bedforms often preserve information of the flow parameters by which they were formed (e.g., Southard, 1991, Soulsby and Clarke, 2005). Ripple-related bed roughness in turn modifies near-bed hydrodynamics and turbulence, ultimately affecting sediment fluxes, a process which is essential for the modelling of sediment transport (e.g., Soulsby, 1997, Van Rijn, 2007). Many estuarine and coastal environments face extreme weather events, which are predicted to increase in frequency with rising sea levels (e.g., Woodruff et al., 2013). Storm-induced waves combined with currents cause particularly dynamic ripple behaviour, and thus high and rapidly changing sediment transport rates (e.g., Li and Amos, 1999, Wengrove et al., 2018). The understanding of how hydrodynamics control ripple dimensions is therefore essential for ensuring the improved performance of coastal morphodynamic models through well-parameterised bed roughness. This is also beneficial for the improvement of estuarine and coastal management and the broader understanding the impact of climate change and sea level rise on coastal systems. Furthermore, using inverse relationships to predict hydrodynamic variables from ripples preserved in sedimentary rocks is essential for the accurate reconstruction of paleoenvironments (e.g., Rubin and Carter, 2005, Myrow et al., 2018). Finally, in view of the nutrient cycle of the coastal ecosystem, ripples have a significant effect on the exchange of dissolved substances between the water column and the seabed, providing organic matter to benthic communities and returning the decompositional products as nitrogen resources for phytoplankton (e.g., Nedwell et al., 1993, Snelgrove and Butman, 1995, Huettel et al., 1996).

Flume studies have provided high-quality process information concerning ripple dynamics on beds composed of well-sorted clean sand under steady currents (e.g., Baas, 1994, Baas, 1999), waves (e.g., Pedocchi and García, 2009, O'Hara Murray et al., 2011), and combined wave and

current flows (e.g., Dumas et al., 2005, Perillo et al., 2014b). Empirical formulae developed for the prediction of ripple size have been derived from clean sand ripples in laboratories and at field sites (e.g., Khelifa and Ouellet, 2000, Nelson et al., 2013, Lapotre et al., 2017). However, these ripple size predictors are of limited use for the majority of estuarine and coastal environments, where sediment almost universally consists of mixture of cohesive clay and non-cohesive sand (Healy et al., 2002). Recently, researchers have therefore focused on ripple dynamics within substrates composed of mixtures of sand and clay. For steady currents with a depth-averaged velocity of  $\sim 0.36$  m/s, Baas et al. (2013) found that equilibrium ripple height decreased with increasing initial clay content. Wu et al. (2018) highlighted that a small increase in clay content, from 4.2% to 7.4%, exponentially increased the time needed for ripples to reach equilibrium under waves with a maximum free stream velocity of  $\sim 0.35$  m/s. However, the equilibrium dimensions of these wave ripples were independent of the initial clay content in the bed, up to around 8%. Additionally, clay winnowing, a hydrodynamic sorting process which suspends the finer clay but leaves the coarser sand in the bed (e.g., Cizeau et al., 1999), played a significant role in the transformation of ripples in mixed sand–clay to an increasingly sandy composition in the experiments of Baas et al. (2013) and Wu et al. (2018). Importantly, Baas et al. (2019) has recently highlighted the role of bed cohesion in decreasing current ripple dimensions in the Dee Estuary, U.K., demonstrating that previous laboratory findings are applicable in natural environments. There has, however, been very little research on the dynamics of ripples in mixed sand–clay beds under combined wave-current flows, which are crucial to the sediment dynamics in the majority of estuaries and coastal seas. This paper therefore extends the experimental work of Baas et al. (2013) and Wu et al. (2018) by providing the first results of the influence of cohesive clay on ripple dynamics by means of flume experiments under combined flows. The three specific objectives were: (1) to quantify ripple development rates for different initial bed clay fractions; (2) to determine the relationship

between the equilibrium ripple dimensions and initial bed clay content; and (3) to relate the ripple development to the changing bed composition, based on quantifying clay winnowing from the bed into the water column.

## 2. Methods

A series of large flume experiments were conducted in the Total Environment Simulator at the University of Hull. Three channels of equal size (11 m in length and 1.4 m in width, with brick walls 0.2 m in height) were constructed in a recirculating tank, with a gravel section of one metre in length at the upstream end to allow for boundary layer development and an artificial beach made of polyethylene foam at the downstream end to damp out wave reflections (Figure 1A). A cross-tank mobile gantry centred 3.5 m downstream of the inlet and capable of traversing 2 m downstream held most measurement sensors. A flat sediment bed, 0.1 m thick, was present in each channel at the start of the experiments. Fresh water was used in all experiments, and the water depth,  $h$ , was set to 0.4 m in the test section. Control Run 1 used three beds of well-sorted sand with a median diameter,  $D_{50}$ , of 450  $\mu\text{m}$ . Runs 2 and 3, which considered the effect of physical cohesion, used a homogenous mix of kaolinite clay with  $D_{50} = 8.9 \mu\text{m}$  and the same sand. Six beds were prepared with initial clay content from 5.7% between 12.3% by dry weight (Table 1).

Each run was carried out using combined flows. Flow velocities in each channel were measured by a 25 Hz Vectrino profiler fixed on the gantry beam 4.5 m away from the flume inlet and at 0.12 metres above the initial flat bed (Figure 1A). The monochromatic wave height,  $H$ , and wave period,  $T$  were c. 0.17 m and 2 s, respectively, measured by eight 50 Hz acoustic water level sensors 0.7 m above the still water surface in the tank (Figure 1B). The wave velocity amplitude at the edge of the boundary layer,  $U_o$ , was c. 0.32 m/s, and the depth-averaged current velocity,  $U_c$ , was c. 0.16 m/s. Although there was a small variation in velocities across the

flume tank, this did not significantly influence ripple evolution (Table 1). The waves in the experiments were skewed shallow-water waves with sharp crests and long troughs, generating a maximum combined flow velocity,  $U_{max}$ , of c. 0.45 m/s and a minimum combined flow velocity,  $U_{min}$ , of c. -0.01 m/s at a height above the bed of 0.05 m, when combined with the current (Table 1). Closer to the bed, using the approach of Malarkey and Davies' (2012) strongly non-linear option for calculating the mean bed shear stress,  $\tau_m$ , and maximum bed shear stress,  $\tau_{max}$ , associated with a skin friction roughness of  $2.5D_{50}$  ( $z_0 = 2.5D_{50}/30$ , where  $z_0$  is the theoretical height of zero velocity) in wave–current flow determined from  $h$ ,  $U_o$ ,  $T$  and  $U_c$ , gives  $\tau_{max} = 1.41$  Pa and  $\tau_m = 0.14$  Pa. The minimum bed shear stress,  $\tau_{min} = \tau_m - \tau_{max}$ , was -1.27 Pa, indicating that bed shear stress was far more symmetric in the two wave half cycles than velocity higher up in the flow.

The clay was homogeneously mixed into the sand using a handheld plasterer's mixer inside each channel flattened using a wooden leveller, and scanned using a terrestrial 3D laser scanner (FARO Focus3D X330). At the start of each experiment, syringe-type sediment cores with a diameter of 20 mm and a maximum length of 90 mm were collected from six locations at one-metre intervals along the centre lines of the mixed sand–clay sections. A homogenous sand–clay mix was present in all channels (Figure 5A, G, N), except for one substrate in Run 2, Channel 1, which was therefore excluded from the results presented below.

Bedform evolution was recorded in three dimensions using a Seatek 2MHz Ultrasonic Ranging System (URS) mounted on the gantry 4 m downstream of the flume inlet and 0.3 m above the bed. The URS contained 32 probes spatially distributed across the three channels (16 across Channel 2 and 8 across Channels 1 and 3). The array scanned at a fixed location during the flow and every time the flow was stopped, over an area two metres in length via an auto-traverse system that had a speed of 1 mm/s (Figure 1).

Bed scanning was conducted at pre-set time intervals, gradually increasing from a 5 min interval in the initial phases of the runs, up to 180 min in the later phases of the experiments. Sediment syringe cores from the mixed clay and sand sections were also collected during the experiments whilst waves and currents were stopped. In Run 2, sediment cores were collected at two locations within the 2-metre scan swathe: near the start and near the end. One more collection location from the middle of the swathe was added in Run 3 because ripples with lower clay content were expected to develop faster and an additional sampling point could be beneficial to quantify winnowing. At each collection location, one core was taken from the initial flat bed and as soon as ripples were identified with the URS, a core was collected from the crest and a consecutive trough. After each experiment, the water was drained slowly from the tank and the rippled bed was scanned with the 3D laser scanner, and sediment cores from neighbouring ripple crests and troughs were also collected. Additionally, sediment cores were collected from the ripples in the downstream clean sand section in order to quantify the amount of clay that had re-entered the sandy substrate from being in suspension. All sediment cores were stored in a cold store at a temperature of 4°C prior to grain size analysis using a Malvern Mastersizer 2000. The sediment cores from the initial flat bed and from the ripple troughs were sliced into 10 mm intervals for the grain size analysis; the cores obtained from the ripple crests were sliced in 5 mm intervals to provide higher resolution of the clay content within the ripples. Ripple wavelengths,  $\lambda$ , and heights,  $\eta$ , were determined from the bed elevation profiles (BEP), recorded by each URS sensor. The removal of spikes from the raw BEPs was based on  $dz > dz_m$ , where  $dz$  is the vertical distance between consecutive data points in the BEP and  $dz_m$  is the average vertical distance in the BEP (Van der Mark et al., 2008). Each BEP was then smoothed using a three-point moving average, followed by applying MATLAB® ‘peaks and troughs’ tool to identify the locations of ripple crests and troughs. The end-of-experiment cross-



sectional shape of the ripples was characterized by calculating the ripple steepness (RS) and ripple symmetry index (RSI):

$$RS = \eta/\lambda \quad (1)$$

$$RSI = \lambda_s/\lambda_l \quad (2)$$

where  $\lambda_s$  and  $\lambda_l$  are the length of the stoss side and lee side, respectively. RSI values between 1 and 1.3 denote symmetrical ripples and RSI values higher than 1.5 represent increasingly asymmetrical ripples. Ripples are quasi-asymmetrical for  $1.3 < RSI < 1.5$  (Perillo et al., 2014a).

Furthermore, the mean values of  $\lambda_t$  and  $\eta_t$  at a bed scanning time  $t$  were calculated from all ripples in the BEPs in each channel, in order to construct development curves of ripple wavelength and height. Equilibrium ripple wavelength,  $\lambda_e$ , and height,  $\eta_e$ , and the time required to reach equilibrium wavelength,  $T_\lambda$ , and height,  $T_\eta$ , were calculated using best-fit equations proposed by Baas et al. (2013), which include a delay time for the first appearance of ripples on the flat bed,  $t_i$ :

$$\frac{\lambda_t - \lambda_i}{\lambda_e - \lambda_i} = 1 - 0.1 \frac{t-t_i}{T_\lambda-t_i} \quad (3)$$

$$\frac{\eta_t}{\eta_e} = 1 - 0.1 \frac{t-t_i}{T_\eta-t_i} \quad (4)$$

where  $\lambda_e$ ,  $\eta_e$ ,  $T_\lambda$ ,  $T_\eta$ ,  $\lambda_i$ , and  $t_i$  are fitting coefficients, and  $\lambda_i$  is the initial wavelength of the first ripples that appeared on the flat bed in each run. In this study, the equilibrium time was defined as the time taken for the ripple wavelength or height to reach 90% of its equilibrium value (cf.,

Baas et al., 2013). The coefficient  $t_i$  was zero in the control run with clean sand (Table 2). All the fitting coefficients for the combined flow ripples are listed in Table 2 and discussed in section 3. Finally, characteristic ripple height growth rate,  $r_\eta$ , and wavelength growth rate,  $r_\lambda$ , over the experiment were estimated as follows:

$$r_\eta = \eta_e / T_\eta \quad (5)$$

$$r_\lambda = (\lambda_e - \lambda_i) / T_\lambda \quad (6)$$

**Table 1. Experimental parameters**

Run	Duration (min)	Channel*	$C_0$ (%)	$U_o$ (m/s)	$U_c$ (m/s)	$U_{max}$ (m/s)	$U_{min}$ (m/s)
1	1970	2	0	0.32	0.16	0.45	-0.01
2	2000	2	10.6	0.31	0.15	0.44	-0.01
		3	12.3	0.33	0.20	0.51	-0.01
3	1250	1	5.7	0.32	0.19	0.4	-0.08
		2	8.5	0.31	0.16	0.45	-0.01
		3	11.6	0.33	0.19	0.50	-0.01

\* Data for channel 1 of Run 2 is excluded because clay and sand were not mixed homogeneously.

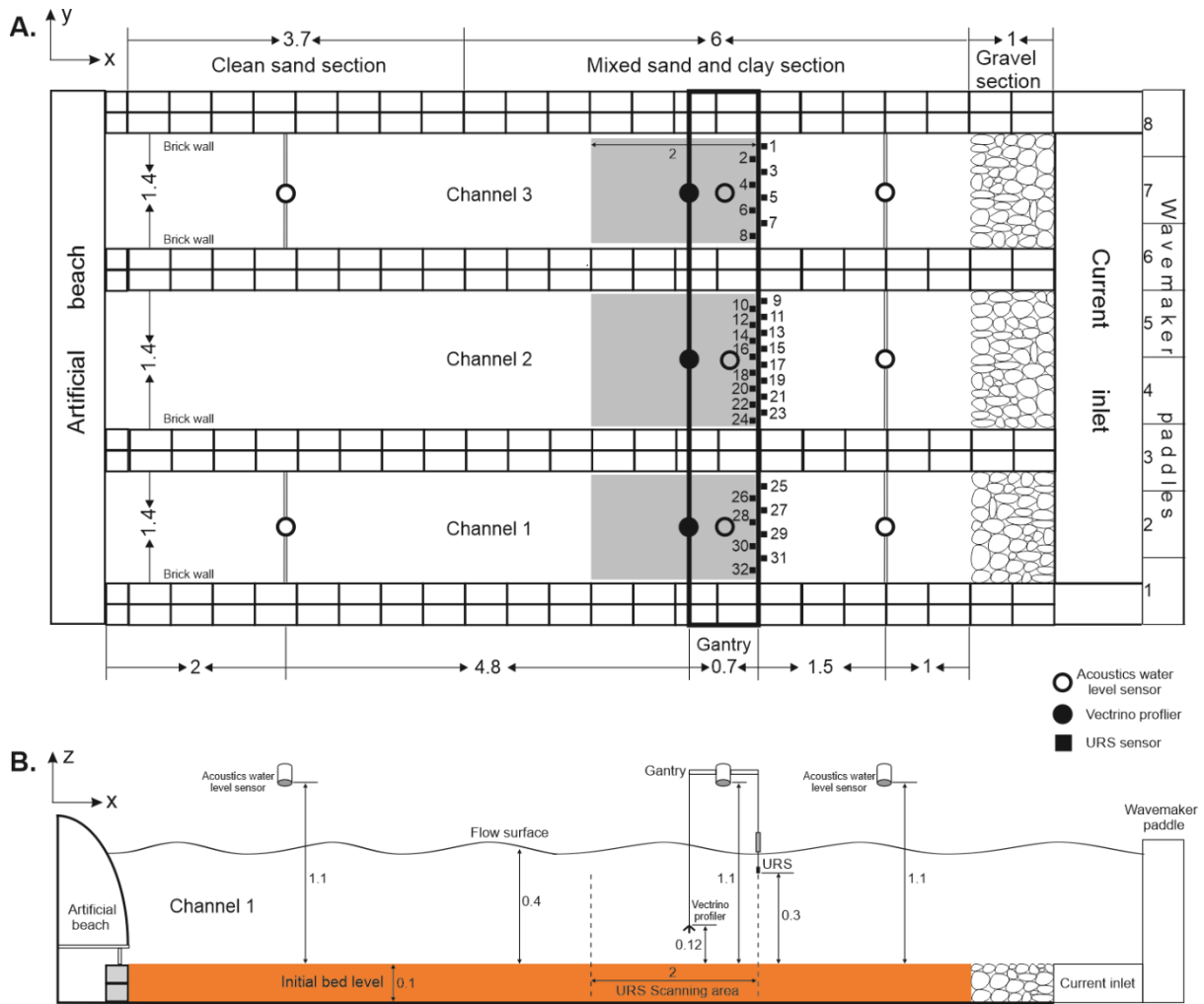


**Figure 1. (A) Plan view and (B) Side view of the experimental set-up. The grey area is scanned by an Ultrasonic Range System (URS) with numbered sensors (black squares). White and black circles denote acoustic water level sensors and Vectrino profilers, respectively. Dimensions are in metres.**

## 3. Results

### 3.1. Ripple development

During the control run ( $C_0 = 0\%$ ), small ripples appeared on the flat bed immediately after the hydrodynamic forcing was applied, as evidenced by a five-min period of rapid growth, during which the mean ripple wavelength and height reached 88.1 mm and 7.2 mm, respectively. Thereafter, the ripple growth rate progressively declined until the ripples stabilised (Figure 2A, B). The development of these ripples exhibited a general trend similar to that reported in the combined flows experiments of Perillo et al. (2014). Equations 3 and 4 revealed that the ripples took 170 min and 90 min to reach an equilibrium wavelength and height of 123.6 mm and 14.6 mm, respectively (Table 2). These fully developed ripples were two-dimensional in planform geometry, characterised by straight, continuous ripple crestlines (Figure 3A). The majority of the ripples were symmetrical or quasi-asymmetrical, with a mean ripple symmetry index of 1.4 and a mean steepness of 0.12 (Table 2), indicating that they were similar to wave-generated vortex ripples.

**Table 2. Ripple parameters**

Run	Channel	$C_0$ (%)	$\eta_e$ (mm)	$\eta_e$ SD (mm)	$\eta_{end}$ (mm)	$T_\eta$ (min)	$r^2$	$\lambda_e$ (mm)	$\lambda_e$ SD (mm)	$\lambda_i$ (mm)	$\lambda_i$ SD (mm)	$\lambda_{end}$ (mm)	$T_\lambda$ (min)	$r^2$	$t_i$ (min)	RSI	RSI SD	RS	RS SD
1	2	0	14.43	1.82	14.61	90	0.78	123.6	4.9	80.7	10.8	124.6	170	0.94	-	1.4	0.3	0.12	0.02
2	2	10.6	14.18	1.16	15.90	834	0.95	110.8	4.0	73.3	11.4	111.4	455	0.85	60	1.3	0.3	0.14	0.03
	3	12.3	3.50	0.31	4.25	211	0.79	98.0	1.7	71.7	6.3	98.7	722	0.93	120	1.5	0.5	0.04	0.02
3	1	5.7	14.72	1.10	15.60	125	0.74	126.5	3.5	91.3	6.3	132.0	330	0.88	5	1.4	0.3	0.12	0.02
	2	8.5	14.32	0.96	14.46	432	0.96	121.4	5.1	80.2	11.6	127.5	456	0.85	60	1.4	0.3	0.11	0.02
	3	11.6	4.10	0.43	5.04	271	0.76	108.5	2.6	84.5	10.0	112.8	382	0.78	90	1.5	0.5	0.05	0.03

$\eta_{end}$ : Mean ripple height at the end of the experiments.

$\lambda_{end}$ : Mean ripple wavelength at the end of the experiments.

$r^2$ : Squared correlation coefficient of the best fit curve.

SD: Standard deviation.

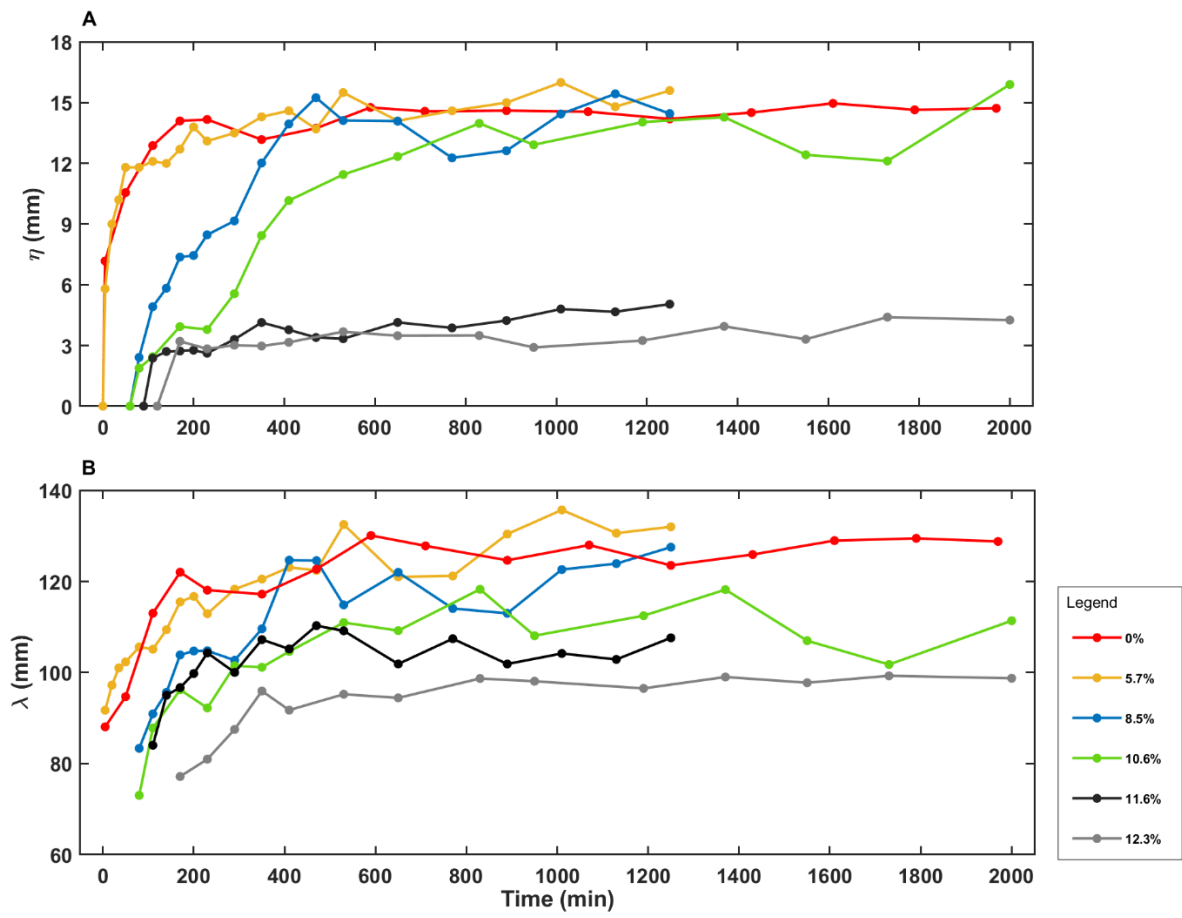


**Figure 2. Development curves for (A) ripple height and (B) ripple wavelength.**

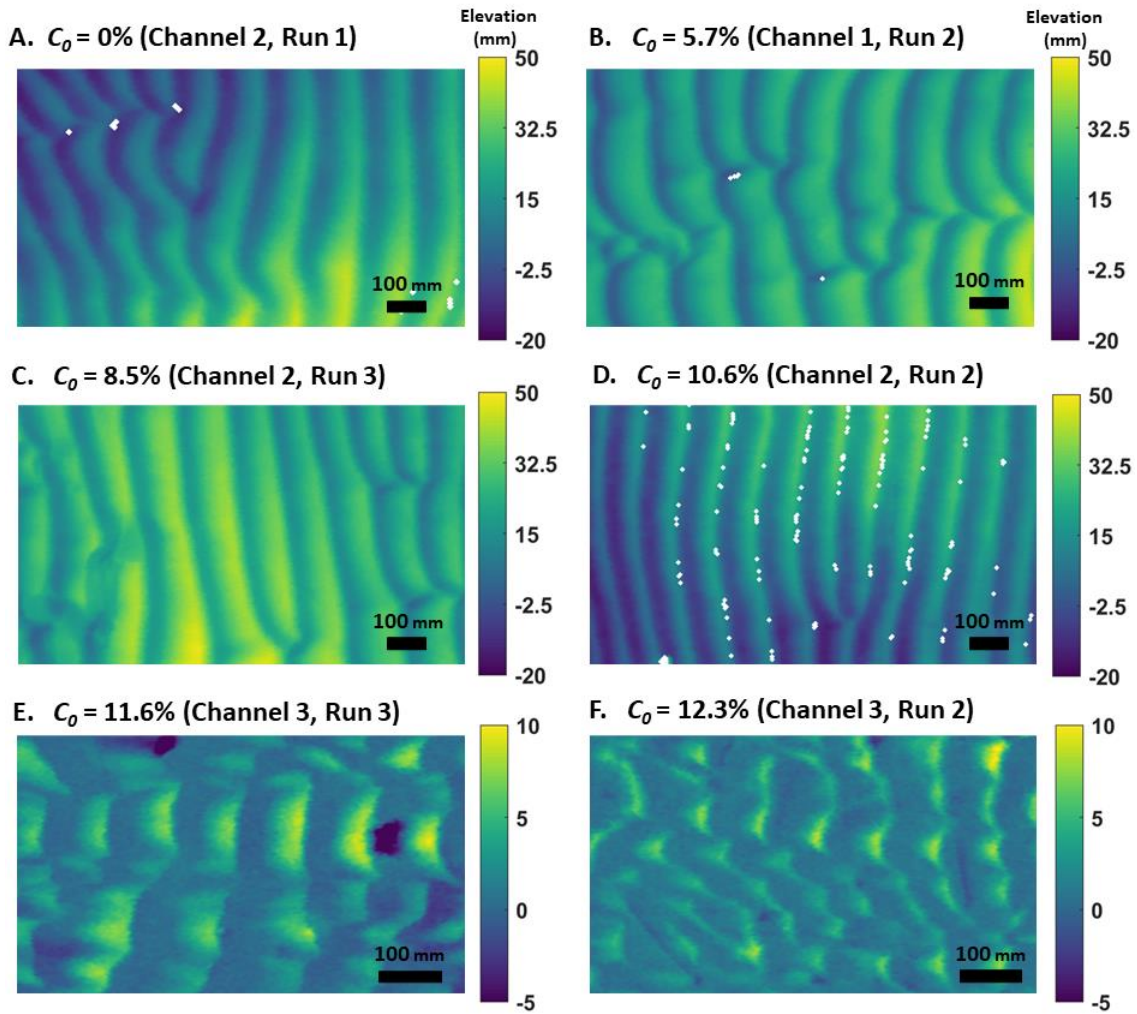


**Figure 3. Plan view of the ripple morphology at the end of the experiments in the test section.  $C_0$  is the initial bed clay content.**

The ripples for the lowest bed clay content,  $C_0 = 5.7\%$  (Run 3, Channel 1), had a similar growth rate to that of the clean-sand ripples in the first 50 min (Figure 2). Thereafter, the ripple growth rate significantly reduced compared to the counterpart in clean sand, such that it took longer to reach equilibrium: 125 min for the ripple height and 330 min for the ripple wavelength. The equilibrium dimensions,  $\eta_e = 14.7$  mm and  $\lambda_e = 126.5$  mm, were similar to the clean-sand ripples, as was their morphology, with two-dimensional ripples covering the bed (Figure 3B).

As  $C_0$  was increased,  $t_i$  increased from 60 min to 120 min (Figure 2; Table 2). Increasing the clay content also slowed the subsequent ripple development (Figure 2). This is particularly clear for  $C_0 = 10.6\%$ , for which the mean ripple height and wavelength were 3.8 mm and 92.2 mm at  $t = 230$  min, compared to 14.2 mm and 118.1 mm for the clean-sand ripples at the same point in time. Thereafter, ripple height experienced a period of relatively rapid, yet gradually decelerating, growth in the following ten hours, reaching  $\eta_t = 10.2$  mm at  $t = 410$  min and  $\eta_e = 14.2$  mm at  $T_\eta = 834$  min (Table 2), which was similar to the equilibrium height of the clean-sand ripples. Ripple wavelength reached equilibrium at  $\lambda_e = 110.8$  mm at  $T_\lambda = 455$  min (Figure 2; Table 2). Not only the dimensions of the ripples were similar to the clean-sand ripples for  $C_0 \leq 10.6\%$ , but these ripples were also two-dimensional, tended to be slightly asymmetrical, with  $RSI \approx 1.3$ , and they had  $RS = 0.11-0.14$  (Figure 3C – D; Table 2).

On beds with 11.6% and 12.3% clay, the mean ripple height was 2.4 mm at  $t = 110$  min and 3.2 mm at  $t = 170$  min (Figure 2), followed by periods of weak growth in the remainder of the experiments. At these bed clay contents, the ripples were unable to develop to sizes similar to the clean-sand ripples, reaching  $\eta_e = 4.1$  mm and  $\eta_e = 3.5$  mm at  $T_\eta = 271$  min and  $T_\eta = 211$  min, with robust confidence of the best fit curve,  $r^2 = 0.78$  and  $0.93$ , respectively (Table 2). These high clay contents also hindered ripple wavelength development. On the bed with 11.6% clay, 280 min were required to reach  $\lambda_e = 108.5$  mm, whereas a longer period of 499 min was needed to reach a shorter  $\lambda_e = 98$  mm on the bed with 12.3% clay. These differences in ripple dynamics, compared to the clean-sand ripples, were also reflected in their geometry. For  $C_0 = 11.6\%$ , the ripples were quasi-2D, characterised by straight but discontinuous crestlines, whereas barchan-shaped ripples with discontinuous crestlines were observed for  $C_0 = 12.3\%$  (Figure 3E - F). Both these ripple types were more asymmetric, with  $RSI = 1.5$ , and markedly flatter, with  $RS \approx 0.05$ , than the clean-sand ripples (Table 2).



Figure 4 illustrates the relationship between the initial clay content and the principal properties of the equilibrium combined-flow ripples. The equilibrium ripple height was almost independent of the initial clay content for  $C_0 \leq 10.6\%$ , at  $\eta_e \approx 14.4$  mm, whereas  $\eta_e$  collapsed to 3.5 mm at the highest  $C_0$  of 12.3%, almost four times smaller than the clean-sand equilibrium height (Figure 4A). The equilibrium wavelength was between 121.4 mm and 129.1 mm for  $C_0 \leq 8.5\%$ , and declined linearly at higher  $C_0$  values, i.e., from 110.8 mm at 10.6% to 98 mm at 12.3% (Figure 4B). The mean growth rate decreased gradually between 0% and 12.3% clay (Figure 4C, D). In the clean-sand run,  $r_\eta$  and  $r_\lambda$ , were 0.003 mm/s and 0.004 mm/s, respectively. At  $C_0 = 12.3\%$ , the mean growth rates were up to an order of magnitude lower at  $r_\eta = 0.0003$  mm/s and  $r_\lambda = 0.0006$  mm/s.

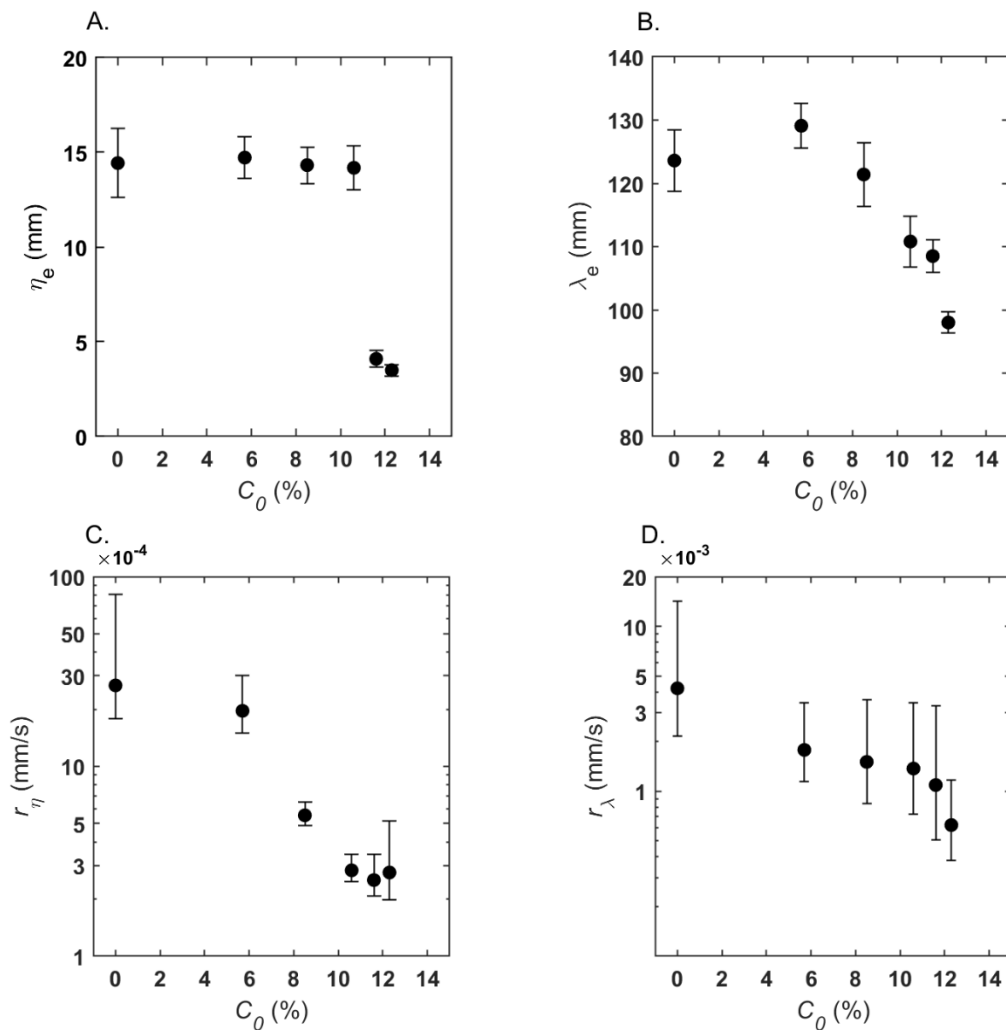


**Figure 4. Equilibrium combined-flow (A) ripple height and (B) wavelength, and development rate of (C) ripple height and (D) wavelength against initial bed clay content for all experiments. Black bars denote 95% confidence intervals, derived from best-fit Equations 3 and 4.**

### 3.2. Change in bed clay content with ripple development

Figure 5 shows representative examples of the changes in bed clay content for different stages in the development of the ripples at  $C_0 = 5.7\%$ ,  $10.6\%$ , and  $12.3\%$ , based on the grain-size analysis of the sediment in the cores. The first profile for  $C_0 = 5.7\%$  was at  $t = 5$  min, when the bed was partly flat and partly occupied by small ripples. In the upper 15 mm of the flat bed core (black line in Figure 5A), the clay content was about half of its initial value (grey vertical solid line in Figure 5A). Below this layer, the clay content increased with depth to its initial value (Figure 5A). The sand was free of clay below the crest of the small, 8 mm high, ripples, whereas a small amount of clay remained at the base of the ripple (blue line in Figure 5A). In a 10-mm thick layer immediately below the ripple trough, the clay content was c. 60% lower than the initial value (red line in Figure 5A). Below this layer, the clay content had remained close to its initial value (Figure 5A). Figure 5B – E illustrate the effect of ripple growth on bed clay content. The clay content in the rippled part of the cores was zero, indicating that the winnowing of clay from the bed kept pace with the growth in ripple height. Furthermore, the thickness of the layer losing clay just below the ripple base progressively expanded downwards until it reached the pre-experiment value at the base of the deposit between 650 min and 1250 min.

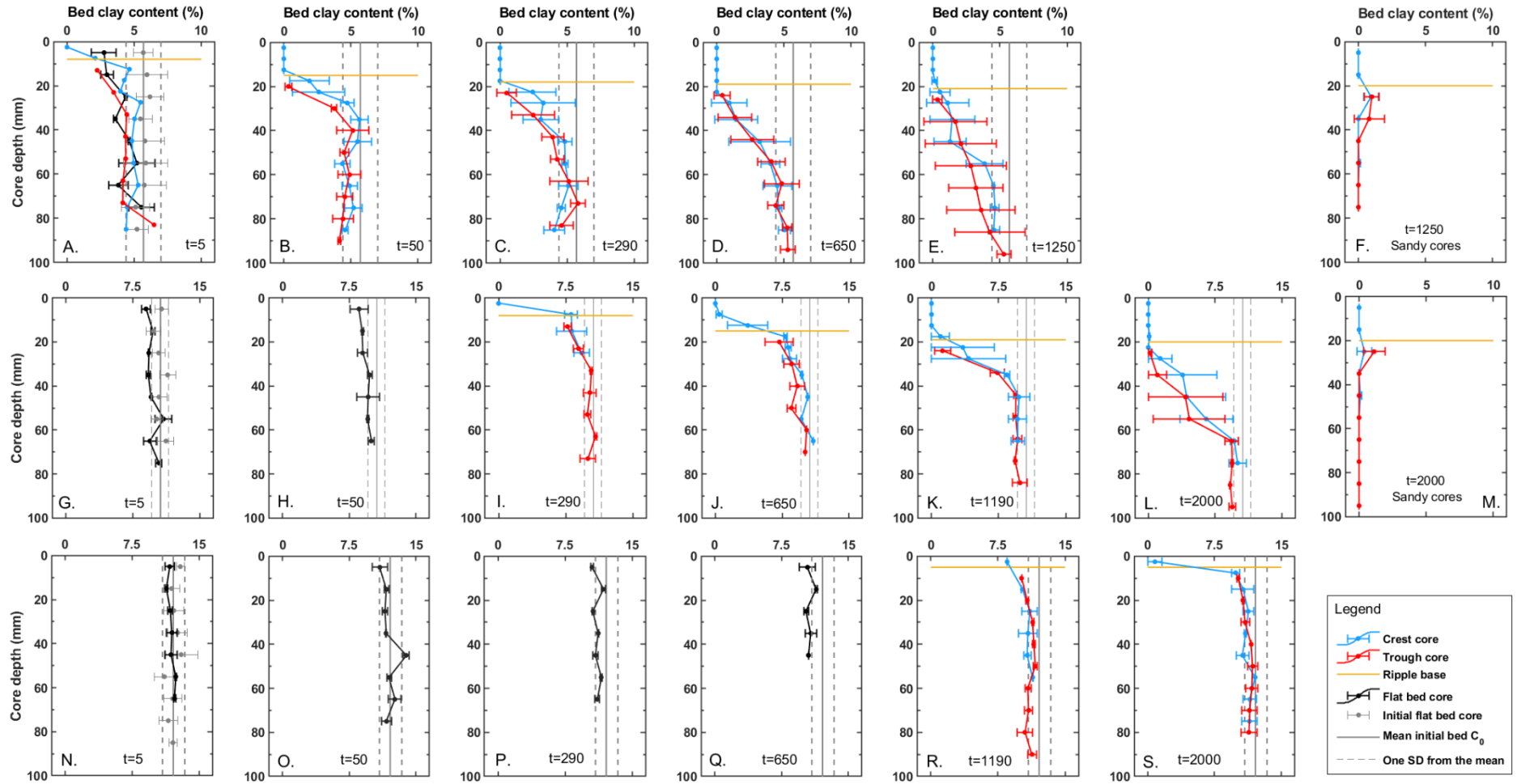


Figure 5. Vertical profiles of clay content in cores collected from beds in the mixed sand–clay section with clay content of (A – E) 5.7%, (G – L) 10.6% and (N – S) 12.3%, and from end-of-experiment rippled beds in the clean sand section downstream in (M) Run 2 and (F) Run 3. The grey dots denote mean initial bed clay content at each

**depth. The grey vertical solid lines and the vertical dash lines represent mean initial clay content and one standard deviation of the mean. The black, blue, and red dots denote mean clay content below the active flat bed, ripple crest, and ripple trough, respectively. The black, blue, and red horizontal bars denote one standard deviation of mean clay content. The yellow lines represent the ripple base and the time,  $t$ , at which the core was taken is in min.**

Five minutes after the start of the run with  $C_0 = 10.6\%$ , the clay content in the top 10 mm of the flat bed core was lower than the initial value, but above 7.5%; this layer of slightly reduced clay content had expanded downward to c. 30 mm at  $t = 50$  min (Figure 5G, H). By  $t = 290$  min, the ripples contained 100% sand just below the ripple crest. Akin to the 5.7% clay run, clay was retained at the ripple base, with a ~10 mm thick layer showing a c. 30% reduction in clay content underneath the ripples (Figure 5I). Compared to  $C_0 = 5.7\%$ , the sediment cores demonstrate a slower evolution towards fully developed sandy ripples in conjunction with a slower downward expansion of the layer with reduced clay content underneath the ripples (Figure 5I – L). Figure 5F and 5M show vertical profiles of bed clay content collected from ripples in the downstream clean sand section at the end of the experiments. Both profiles reveal clay-free ripples and a clay-enriched layer below the base of the ripples. This layer was c. 20 mm thick at  $C_0 = 5.7\%$  and c. 10 mm thick at  $C_0 = 10.6\%$ .

The bed clay content in the run with  $C_0 = 12.3\%$  was close to the initial value at  $t = 5$  min (Figure 5N). At  $t = 50$  min, the upper 10 mm of the bed had lost a small amount of clay; ripples had not formed at this stage (Figure 5O). Tiny ripples were present at  $t = 290$  min and  $t = 650$  min, but it was not possible to sample through the crests and troughs of these ripples. Bed clay content in the upper 10 mm had continued to decrease at these times (Figure 5P, Q). Draining the tank at  $t = 1190$  min and  $t = 2000$  min revealed small, c. 5 mm high, ripples. These ripples had retained 8.5% clay at  $t = 1190$  min, but only 0.8% at  $t = 2000$  min. Again, a thin layer of reduced clay content was present just below the base of the ripples, in which the clay content gradually recovered downward to its initial value, but the initial value was reached at shallower depths than in the runs with lower initial bed clay content (Figure 5R, S).

## 4. Discussion

### 4.1. Ripple development on cohesive substrates under combined flows

The experimental results described in this paper illustrate the role of cohesive sediment in changing the dynamics of combined-flow ripples by slowing the ripple growth rate (Figure 4C, D; cf. Baas et al., 2013; Wu et al., 2018). For beds with  $C_0 \leq 10.6\%$ , the ripples developed to a comparable equilibrium shape and size, with  $\eta_e \approx 14.4$  mm and  $\lambda_e \approx 123.8$  mm, but the cohesive forces caused the equilibrium time to increase exponentially as  $C_0$  was increased from 0% to 10.6% (Table 2). These observations are consistent with the findings of Wu et al. (2018), who studied the development of wave ripples on sand beds with up to 7.4% kaolinite clay. However, Baas et al. (2013) described a small decrease in height and a constant wavelength of current ripples, as  $C_0$  was increased from 0% to 12.6%, and Baas et al. (2013) found a similar equilibrium time for all ripples independent of bed kaolinite content. The relatively short duration of 2 hours used in the experiments of Baas et al. (2013) may have prevented the best-fit equations (cf. Equations 3 and 4) from predicting sufficiently accurate equilibrium times, especially at  $C_0$  values between 7% and 12.6%. This viewpoint is supported by the experiments with mixtures of sand and biologically cohesive extracellular polymeric substances (EPS) of Malarkey et al. (2015), whose flow and sand properties were similar to those of Baas et al. (2013), but their runs lasted between 4 and 73 hours. Malarkey et al. (2015) concluded that current ripples developing on beds with EPS contents ranging from 0.016% to 0.125% reached similar equilibrium size and geometry as EPS-free current ripples, provided that sufficient time was allowed for their formation.

The two strongest levels of bed cohesion ( $C_0 = 11.6\%$  and  $12.3\%$ ) used herein not only led to greatly reduced ripple dimensions ( $\eta_e < 5$  mm,  $\lambda_e < 108$  mm), but also to significantly different ripple geometries. At  $RS = 0.04$ , these small ripples resemble rolling-grain ripples without flow

separation at the crest, as opposed to vortex ripples with flow separation that require  $RS > 0.1$  (Miller and Komar, 1980). Rolling-grain ripples are associated with steady circulation cells on either side of the ripple crest (Hara and Mei, 1990), which drive sediment towards the crest, causing the ripple to grow until it is steep enough for flow separation and periodic vortex shedding to begin (e.g., van der Werf et al., 2008). Perillo et al. (2014b) identified small and two-dimensional rolling-grain ripples on clean sand beds under combined flows. However, the rolling-grain ripples at  $C_o = 12.3\%$  in the present study were barchan-shaped (Figure 3F). It is likely that the stronger cohesion within the bed at  $C_o = 12.3\%$  prevented these ripples from evolving into the two-dimensional ripples with discontinuous crestlines of  $C_o = 11.6\%$  or even the straight-crested and continuous ripple trains of  $C_o \leq 10.6\%$ .

Previous experiments have found that clean-sand rolling-grain ripples are a transitional and unstable stage towards equilibrium vortex ripples (Scherer et al., 1999, Stegner and Wesfreid, 1999, Faraci and Foti, 2001). This transition is usually a rapid process. In the clean-sand experiments of Faraci and Foti (2001), rolling-grain ripples lasted less than 240 seconds before developing into vortex ripples at  $U_o = 0.43$  m/s. In our experiments, however, the rolling-grain ripples were stable for over 20 hours (Figure 2). We therefore infer that an equilibrium state – or at least a prolonged metastable state – for these ripples is possible in mixed sand–clay. The sudden increase in physical cohesion in the bed as increasing  $C_o$  may have limited the supply of sand from below the base of the ripples, thus keeping the ripples small enough to become fixed in the rolling-grain ripple stage. Faraci and Foti (2001) demonstrated a short transient period of stalling in the growth of rolling-grain ripple height towards vortex ripples. A similar but much longer period of stalling was observed at  $C_o = 10.6\%$  in the present experiments; the ripple height remained at c. 4 mm at  $170 < t < 230$  min, followed by continued growth towards equilibrium when the clay content immediately below the ripple troughs decreased below 8% (Figure 2; Figure 5I). A clay content of 8% may therefore be a threshold below which growth

towards the equilibrium size typical of clean-sand ripples is able to occur, and ripples develop separation eddies typical of vortex ripples. Bed clay content above 8% thus prevent the circulation cells from supplying enough sand from the troughs to allow the ripples to grow and the flow to separate, so the rolling-grain ripples persist. This threshold was never passed in 12.3% clay run, since the clay content below the base of the ripples remained at 10% or above consistently (Figure 5R, S), resulting in the persistence of rolling-grain ripples until the end of the experiment. Further research designed to quantify the clay-content threshold for the change from rolling-grain to vortex ripples under different forcing conditions is required to fully understand the influence of cohesive clay on ripple evolution and equilibrium ripple size and shape. Interestingly, Baas et al. (2013) also found a drastic reduction in the size of current ripples in runs with over 13% bed clay, with heights and wavelengths lower than 5.5 mm and 80 mm. These ripples were two-dimensional and flatter than the three-dimensional, linguoid, equilibrium clean-sand ripples ( $RS \approx 0.05$  versus  $RS \approx 0.13$ ; Baas et al., 2013). Most significantly, once formed these small current ripples were stable until the end of the experiments.

It is therefore concluded that two distinct types of equilibrium wave, current, and combined flow ripples are able to develop on mixed sand–clay beds, with the conceptual models of these two types of ripple development shown in Figure 6. If  $C_0$  is lower than the threshold bed clay concentration,  $C_t$ , relatively large equilibrium ripples, with dimensions and geometries comparable to clean-sand counterparts, are developed. These ripples experience similar development stages as those of clean-sand ripples, including incipient, growing, and equilibrium stages (Perillo et al., 2014b; Figure 6A – D), although the growth rate is lower than that of the clean-sand ripples. Relatively small and flat equilibrium ripples are generated as  $C_0 > C_t$  (Figure 6E – H). Incipient ripples that appear after an extended period of flat bed conditions



because of high bed cohesion, are unable to grow to large sizes because of a lack of sand supply from below (Figure 6G – H).

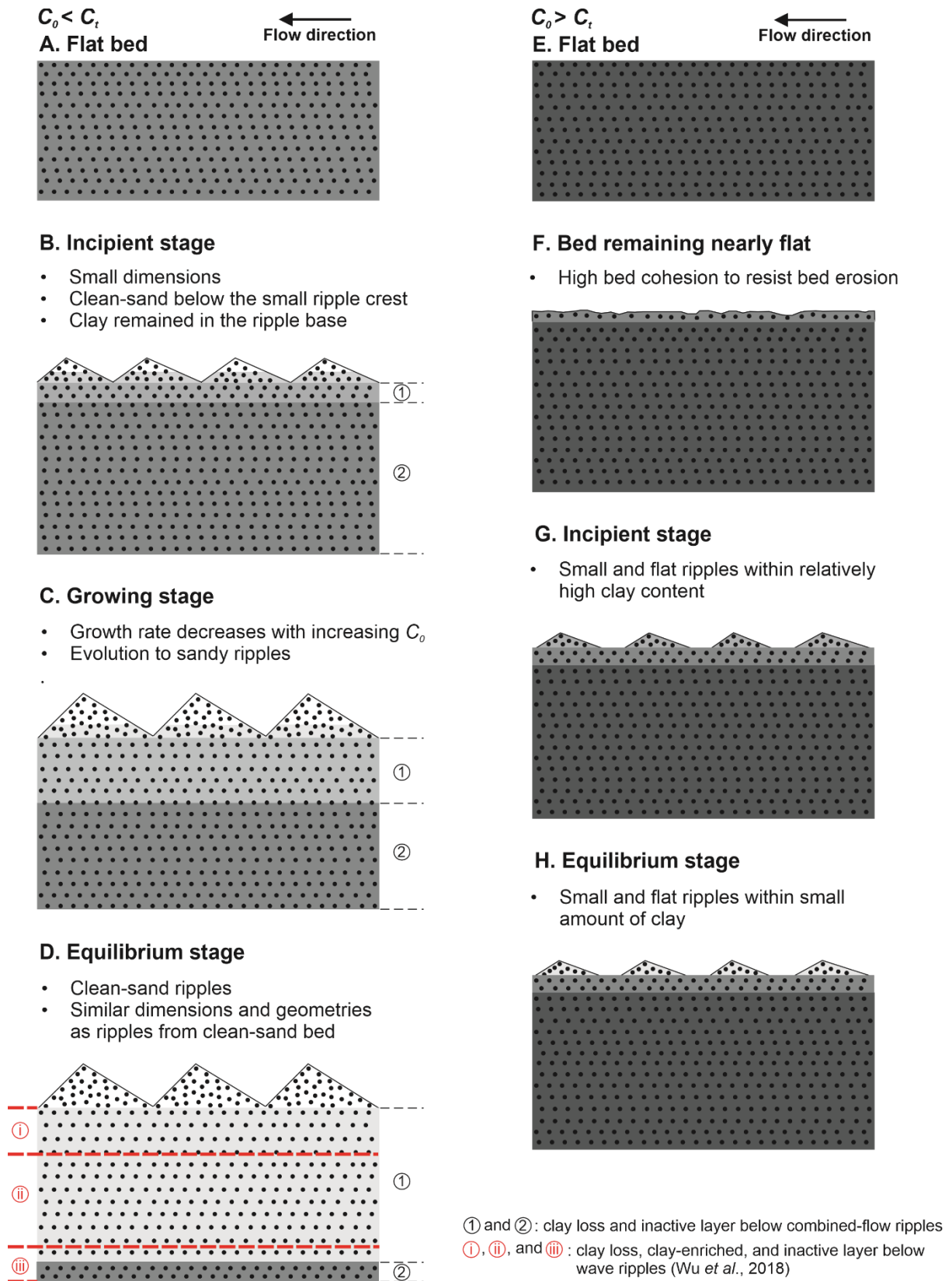


**Figure 6. Conceptual models showing the development stages of (A - D) large and (E - F) small equilibrium ripples under currents, waves, and combined flows.  $C_t$ : threshold bed clay content. The horizons with different clay fractions are presented by different shades of grey. Red dash lines represent boundaries of sediment layers below the wave ripples of Wu et al. (2018).**

#### 4.2. Influence of clay winnowing on ripple development

The present experiments, as well as previous flume studies (e.g., Malarkey et al., 2015, Wu et al., 2018), indicate that the equilibrium dimensions of ripples on weakly cohesive, mixed sand–clay beds are similar to those of their clean-sand equivalents, but that these ripples may take an exponentially longer time to reach equilibrium than clean-sand ripples. Our core data confirm earlier findings that winnowing of fine, cohesive material, i.e., clay and EPS, from the active surficial sediment layer leads the transformation of a cohesive bed to sandy ripples (Baas et al. 2013; Wu et al., 2018). During winnowing, small clay particles (and EPS) are preferentially resuspended from the bed because of their low critical entrainment velocity (Allan and Frostick, 1999). Winnowing therefore plays a significant role in bed coarsening (Blom et al., 2003, Liang et al., 2007). Winnowing of clay occurs preferentially by hyporheic flow below ripple troughs (Blom et al., 2003), thus supplying sand from underneath the base level of ripples to assist ripple growth. However, hyporheic flows, and therefore winnowing, can get blocked when the bed clay content is sufficiently high to fill the pore space (Niño et al., 2003, Staudt et al., 2017). In the present experiments, the increase in bed clay content from 5.7% to 12.3% is inferred to have caused a progressive decrease in the rate of winnowing of clay by hyporheic flow, in combination with a progressive increase of critical bed shear stress for sediment motion with increasing bed clay content (e.g., Panagiotopoulos et al., 1997). Hence, the ripple growth rate decreased with increasing bed clay content, because the rate of clay winnowing decreased, in turn leading to a reduced supply of sand needed for ripple growth.

Wu et al. (2018) recognised layers enriched in clay relative to initial bed clay content below equilibrium wave ripples (Figure 6D). The sediment below the combined-flow ripples in our cores did not record such layers, with clay loss layers instead dominating sedimentary texture during ripple development (Figure 6A – D). However, clay did accumulate between 25 and 35 mm in the sandy section downstream of the mixed sand–clay beds (Figure 5F, M). This provides further evidence that suspended clay can be carried into rippled beds by hyporheic flow, driven by pressure gradients between ripple troughs and crests (e.g., Huettel et al., 1996, Karwan and Saiers, 2012, Wu et al., 2018, Dallmann et al., 2020). Clay probably also entered the rippled beds in the mixed sand–clay test section, as evidenced by plateaus of increased clay content immediately below the ripple base, e.g., between 22.5 and 45 mm and between 35 and 55 mm at the end of Runs 3 and 2, respectively (Figure 5E, L). These depths are similar to the depths at which clay accumulated in the downstream sandy area and in the wave-ripple experiments of Wu et al. (2018; their figure 11). There therefore appears to be a dynamic balance between clay loss and gain below the base of the ripples. Clay gain by downward movement was higher than clay loss by upward winnowing below the base of the wave ripples, causing net clay accumulation at this depth, whereas winnowing-induced clay loss was dominant in the present combined-flow experiments, thus causing ‘deep cleaning’ of bed clay (Figure 6D). This suggests that winnowing was stronger under the combined-flow forcing herein than under the pure wave forcing of Wu et al. (2018). Currents with superimposed waves are well known to generate high turbulence intensities and shear stresses in the wave boundary layer, resulting in apparent bed roughness lengths that are much greater than the sum of their constituents (Grant and Madsen, 1979, Mathisen and Madsen, 1996). Indeed, based on the Malarkey and Davies (2012) shear stress calculation method, the maximum skin friction shear stress in the present experiments was 1.41 Pa, c. 40% higher than under the pure wave conditions with similar free-stream maximum orbital velocities of Wu et al. (2018). Hence,

combined flow has the capacity to induce stronger forces to winnow more clay from rippled mixed sand–clay beds than pure oscillatory flow. Moreover, hydrodynamic forces control hyporheic flows through the bed, i.e., pore water velocity scales positively with flow velocity (Elliott and Brooks, 1997, Karwan and Saiers, 2012). Clark et al. (2019) highlighted that combined flow produced a deeper hyporheic exchange than that induced by currents alone due to ‘wave pumping’ effect. Furthermore, Packman et al. (2000) developed a method for the calculation of pore water velocity,  $u_p$ , in a rippled bed:

$$u_p = kKh_m \quad (7)$$

where  $k = 2\pi/\lambda$  is the hydraulic conductivity,  $K = 600D_{10}^2$ ,  $D_{10}$  is the 10-percentile of the grain-size distribution,  $h_m = 0.14(U^2/g)(\eta/0.34h)^{3/8}$  is the half-amplitude dynamic head,  $g$  is gravitational acceleration, and  $U$  is the root-mean square flow velocity (Precht and Huettel, 2003). For  $U = 0.31$  m/s and  $D_{10} = 0.3$  mm in the present experiments,  $u_p = 1.5$  mm/min, whereas the pore water velocity was 40% lower, i.e.,  $u_p = 0.9$  mm/min, in the pure-wave experiments of Wu et al. (2018). This higher pore water velocity, combined with the higher bed shear stress, may explain why the clay can be winnowed from deeper levels in the substrate under combined-flow forcing.

### 4.3 Implications for natural environments

The present experiments, supported by Baas et al. (2013) and Wu et al. (2018), show that ripple types change into one another across a narrow range of bed clay contents, suggesting a discontinuity in ripple dimensions and geometries that is not incorporated in mathematical predictors for bedform height and wavelength (e.g., Tanaka et al., 1996; Nelson et al., 2013). Because the large equilibrium ripples resemble clean-sand ripples as a result of highly effective clay winnowing, the application of these predictors may be extended from pure sand beds to weakly cohesive mixed sand–clay beds. However, these predictors need to be modified to capture the small equilibrium ripples that are stable only on strongly cohesive beds. This

indicates that bedform predictors developed from clean-sand ripples are likely to overpredict ripple roughness for sand beds with a high bed clay content. Indeed, using  $k_s = 27.7\eta^2/\lambda$  (Li and Amos, 1998), where  $k_s$  is the bed roughness due to form drag, the sudden reduction in ripple dimensions at  $C_o \approx 11\%$  (Figure 4A, B) causes the bed roughness to decrease by an order of magnitude. Brakenhoff et al. (2020) highlighted the fact that small changes in predicted form roughness could result in large changes in sediment transport rate predictions. The data in this study show that such errors may result from neglecting the profound effect of cohesive forces in mixed sand–clay beds, thus limiting the ability of models to accurately predict changes in the bed morphology of estuaries and coastal sea. The discontinuity between large and small combined-flow ripples was at an initial bed clay content of 11% and at a clay content of c. 8% below the base of the ripples. It is expected that these threshold concentrations depend on the maximum combined shear stress, which in nature can be significantly higher than in the present experiments. For example, strong bed shear stresses during extreme weather events might increase the threshold bed clay content below which bedforms in mixed sand–clay beds can attain the size of clean-sand equivalents through clay winnowing. On the other hand, EPS-induced biological cohesion in sediment has a stronger capacity to resist erosion compared to physical cohesion; small proportions of EPS, of the order of 0.1%, are highly effective in hindering bedform evolution (Malarkey et al., 2015, Parsons et al., 2016). This should reduce the cohesion threshold for clean-sand equivalent bedform development in mixed sand–clay-EPS sediment beds in nature and work against the increase in this threshold as a result of the higher bed shear stresses described above. The findings in this paper should act as a stimulus for further studies towards fully quantifying changes in ripple morphology as a function of hydrodynamic forcing and bed cohesion. This would also be helpful for designing the next-generation phase diagrams for combined-flow bedforms, which at present do not cover bed

cohesion and therefore cannot predict the small equilibrium ripples found in this study (Dumas et al., 2005, Perillo et al., 2014a).

Our experiments show that an apparently stable cohesive mixed sand–clay bed can become unstable quickly through highly efficient clay winnowing far below the bed surface. This rapid change from a cohesive substrate to a mobile, predominantly sandy substrate is likely to occur also in natural environments, especially during storm events. This rapid change in bed stability may further challenge the modelling of sediment transport in estuaries, given that river flooding often goes hand in hand with storm events (e.g., Gong et al., 2007, Ralston et al., 2013). Such combined flows would not only lead to clay loss by winnowing under high maximum bed shear stress, but it may also lead to an increased supply into the estuary of suspended terrestrial clay as well as organic matter and toxic chemicals attracted to clay particle surfaces through physicochemical forces (Partheniades, 2009). These materials could become trapped in the estuary, especially during extended periods of calm conditions, given the slow deposit entry rates discussed by Dallmann et al., (2020). During subsequent storms, however, the strong winnowing-induced, ‘deep cleaning’ effect is likely to release large volumes of clay, nutrients, and pollutants back into the water column over a short amount of time, with potentially severe impacts on the health of the estuarine environment. For example, a sudden, large release of nutrients may cause algal blooms (‘red tides’; Brand et al., 2012), and a sudden, large release of contaminants causes near-instantaneous water pollution, threatening the ecological balance of estuarine and coastal environments and anthropogenic activities. The findings of this study are therefore also beneficial for the development of evidence-based water-quality regulations in estuaries.

## 5. Conclusion

Our experiments examined the importance of physical cohesion on the size and morphology of ripples generated by combined waves and currents. The experimental data illustrate that, with initial clay content,  $C_0$ , increasing from 0% to 12.3%, ripple height and wavelength development rates,  $r_\eta$  and  $r_\lambda$  decreased one order of magnitude from 0.003 mm/s to 0.0003 mm/s and from 0.004 mm/s to 0.0006 mm/s, respectively. Importantly, the experimental results also revealed the development of two distinct types of equilibrium ripples on mixed sand–clay beds. For  $C_0 \leq 10.6\%$ , large two-dimensional, quasi-asymmetrical equilibrium ripples developed, with equilibrium height and wavelength,  $\eta_e \approx 14.4$  mm,  $\lambda_e \approx 123.9$  mm, ripple symmetry index,  $RSI \approx 1.4$ , and ripple steepness,  $RS \approx 0.12$ . These geometric values are close to those of clean-sand ripples, because the winnowing of clay from the developing ripples at these low  $C_0$ -values was highly effective — typically amounting to 100% clay loss — and clay winnowing extended far below the ripples during equilibrium bed morphology. This ‘deep cleaning’ of clay is probably attributable to higher bed shear stresses and pore water velocities under combined flow than under pure currents and pure waves. In contrast, high bed cohesion at  $C_0 > 11\%$  led to a discontinuity in equilibrium ripple height, generating small, flat, and more asymmetrical equilibrium ripples, with  $\eta_e$  and  $RS$  collapsing to  $\sim 4$  mm and 0.04, respectively, but  $RSI$  increasing to 1.5. This discontinuity is explained by a sudden increase in bed cohesion as a function of increasing bed clay content, which prevents the erosion of ripple troughs and limits the sand supply needed for the growth towards the larger combined-flow ripples.

## Acknowledgements

The authors acknowledge the enormous contributions of Brendan Murphy, whose help throughout the study made our setup, data collection, and clean-up efforts smooth and trouble-free. We also acknowledge the extremely useful contributions of Ellen Pollard, Dr. Hachem

Kassem, Prof. Stuart McLelland, Dr. Elena Bastianon, Dr. Anne Baar, Dr. Christina Roggatz, and Sojiro Fukuda during different stages of the experiments. Participation of XW, RF, JM and DP was made possible thanks to funding by the European Research Council under the European Union's Horizon 2020 research and innovation program (grant 725955). Participation of RF also supported by the Leverhulme Trust, Leverhulme Early Career Researcher Fellowship (grant ECF-2020-679).

### **Conflict of Interest**

The authors declare no conflicts of interest relevant to this study.

### **Data Availability Statement**

Data supporting the findings of this study have been uploaded to the Pangaea repository but are still undergoing their internal review/moderation. We will update this preprint as soon as the link is available. In the meantime, the data is available through this Box link:

<https://universityofhull.box.com/s/d7drlbt3e6apy4sn9sr5flifuqyxb4ks>



## References

- ALLAN, A. F. & FROSTICK, L. 1999. Framework dilation, winnowing, and matrix particle size; the behavior of some sand-gravel mixtures in a laboratory flume. *Journal of Sedimentary Research*, 69, 21-26.
- BAAS, J. H. 1994. A flume study on the development and equilibrium morphology of current ripples in very fine sand. *Sedimentology*, 41, 185-209.
- BAAS, J. H. 1999. An empirical model for the development and equilibrium morphology of current ripples in fine sand. *Sedimentology*, 46, 123-138.
- BAAS, J. H., BAKER, M. L., MALARKEY, J., BASS, S. J., MANNING, A. J., HOPE, J. A., PEAKALL, J., LICHTMAN, I. D., YE, L. & DAVIES, A. G. 2019. Integrating field and laboratory approaches for ripple development in mixed sand–clay–EPS. *Sedimentology*, 66, 2749-2768.
- BAAS, J. H., DAVIES, A. G. & MALARKEY, J. 2013. Bedform development in mixed sand–mud: The contrasting role of cohesive forces in flow and bed. *Geomorphology*, 182, 19-32.
- BLOM, A., RIBBERINK, J. S. & DE VRIEND, H. J. 2003. Vertical sorting in bed forms: Flume experiments with a natural and a trimodal sediment mixture. *Water Resources Research*, 39.
- BRAKENHOFF, L., SCHRIJVERS, R., VAN DER WERF, J., GRASMEIJER, B., RUESSINK, G. & VAN DER VEGT, M. 2020. From ripples to large-scale sand transport: The effects of bedform-related roughness on hydrodynamics and sediment transport patterns in delft3d. *Journal of Marine Science and Engineering*, 8, 892.
- BRAND, L. E., CAMPBELL, L. & BRESNAN, E. 2012. *Karenia*: The biology and ecology of a toxic genus. *Harmful algae*, 14, 156-178.
- CIZEAU, P., MAKSE, H. A. & STANLEY, H. E. 1999. Mechanisms of granular spontaneous stratification and segregation in two-dimensional silos. *Physical Review E*, 59, 4408.
- CLARK, J. J., QIAN, Q., VOLLER, V. R. & STEFAN, H. G. 2019. Hyporheic exchange in a gravel bed flume with and without traveling surface waves. *Advances in Water Resources*, 123, 120-133.
- DALLMANN, J., PHILLIPS, C., TEITELBAUM, Y., SUND, N., SCHUMER, R., ARNON, S. & PACKMAN, A. 2020. Impacts of suspended clay particle deposition on sand-bed morphodynamics. *Water Resources Research*, 56, e2019WR027010.
- DUMAS, S., ARNOTT, R. & SOUTHARD, J. B. 2005. Experiments on oscillatory-flow and combined-flow bed forms: implications for interpreting parts of the shallow-marine sedimentary record. *Journal of Sedimentary research*, 75, 501-513.
- ELLIOTT, A. H. & BROOKS, N. H. 1997. Transfer of nonsorbing solutes to a streambed with bed forms: Theory. *Water Resources Research*, 33, 123-136.
- FARACI, C. & FOTI, E. 2001. Evolution of small scale regular patterns generated by waves propagating over a sandy bottom. *Physics of Fluids*, 13, 1624-1634.
- GONG, W., SHEN, J. & REAY, W. G. 2007. The hydrodynamic response of the York River estuary to Tropical Cyclone Isabel, 2003. *Estuarine, Coastal and Shelf Science*, 73, 695-710.
- GRANT, W. D. & MADSEN, O. S. 1979. Combined wave and current interaction with a rough bottom. *Journal of Geophysical Research: Oceans*, 84, 1797-1808.
- HARA, T. & MEI, C. C. 1990. Centrifugal instability of an oscillatory flow over periodic ripples. *Journal of Fluid Mechanics*, 217, 1-32.
- HEALY, T., WANG, Y. & HEALY, J.-A. 2002. *Muddy coasts of the world: processes, deposits and function*, Elsevier.
- HUETTEL, M., ZIEBIS, W. & FORSTER, S. 1996. Flow-induced uptake of particulate matter in permeable sediments. *Limnology and Oceanography*, 41, 309-322.
- KARWAN, D. L. & SAIERS, J. E. 2012. Hyporheic exchange and streambed filtration of suspended particles. *Water Resources Research*, 48.
- KHELIFA, A. & OUELLET, Y. 2000. Prediction of sand ripple geometry under waves and currents. *Journal of waterway, port, coastal, and ocean engineering*, 126, 14-22.
- LAPOTRE, M. G., LAMB, M. P. & MCELROY, B. 2017. What sets the size of current ripples? *Geology*, 45, 243-246.

- LI, M. Z. & AMOS, C. L. 1998. Predicting ripple geometry and bed roughness under combined waves and currents in a continental shelf environment. *Continental Shelf Research*, 18, 941-970.
- LI, M. Z. & AMOS, C. L. 1999. Field observations of bedforms and sediment transport thresholds of fine sand under combined waves and currents. *Marine Geology*, 158, 147-160.
- LIANG, H., LAMB, M. P. & PARSONS, J. D. 2007. Formation of a sandy near-bed transport layer from a fine-grained bed under oscillatory flow. *Journal of Geophysical Research: Oceans*, 112.
- MALARKEY, J., BAAS, J. H., HOPE, J. A., ASPDEN, R. J., PARSONS, D. R., PEAKALL, J., PATERSON, D. M., SCHINDLER, R. J., YE, L. & LICHTMAN, I. D. 2015. The pervasive role of biological cohesion in bedform development. *Nature communications*, 6, 1-6.
- MALARKEY, J. & DAVIES, A. G. 2012. A simple procedure for calculating the mean and maximum bed stress under wave and current conditions for rough turbulent flow based on method. *Computers & Geosciences*, 43, 101-107.
- MATHISEN, P. P. & MADSEN, O. S. 1996. Waves and currents over a fixed rippled bed: 2. Bottom and apparent roughness experienced by currents in the presence of waves. *Journal of Geophysical Research: Oceans*, 101, 16543-16550.
- MILLER, M. C. & KOMAR, P. D. 1980. Oscillation sand ripples generated by laboratory apparatus. *Journal of Sedimentary Research*, 50, 173-182.
- MYROW, P. M., LAMB, M. & EWING, R. 2018. Rapid sea level rise in the aftermath of a Neoproterozoic snowball Earth. *Science*, 360, 649-651.
- NEDWELL, D., PARKES, R. J., UPTON, A. & ASSINDER, D. 1993. Seasonal fluxes across the sediment-water interface, and processes within sediments. *Philosophical Transactions of the Royal Society of London. Series A: Physical and Engineering Sciences*, 343, 519-529.
- NELSON, T. R., VOULGARIS, G. & TRAYKOVSKI, P. 2013. Predicting wave-induced ripple equilibrium geometry. *Journal of Geophysical Research: Oceans*, 118, 3202-3220.
- NIÑO, Y., LOPEZ, F. & GARCIA, M. 2003. Threshold for particle entrainment into suspension. *Sedimentology*, 50, 247-263.
- O'HARA MURRAY, R., THORNE, P. & HODGSON, D. 2011. Intrawave observations of sediment entrainment processes above sand ripples under irregular waves. *Journal of Geophysical Research: Oceans*, 116.
- PACKMAN, A. I., BROOKS, N. H. & MORGAN, J. J. 2000. A physicochemical model for colloid exchange between a stream and a sand streambed with bed forms. *Water Resources Research*, 36, 2351-2361.
- PANAGIOTOPOULOS, I., VOULGARIS, G. & COLLINS, M. 1997. The influence of clay on the threshold of movement of fine sandy beds. *Coastal Engineering*, 32, 19-43.
- PARSONS, D. R., SCHINDLER, R. J., HOPE, J. A., MALARKEY, J., BAAS, J. H., PEAKALL, J., MANNING, A. J., YE, L., SIMMONS, S. & PATERSON, D. M. 2016. The role of biophysical cohesion on subaqueous bed form size. *Geophysical research letters*, 43, 1566-1573.
- PARTHENIADES, E. 2009. *Cohesive sediments in open channels: erosion, transport and deposition*, Butterworth-Heinemann.
- PEDOCCHI, F. & GARCÍA, M. 2009. Ripple morphology under oscillatory flow: 2. Experiments. *Journal of Geophysical Research: Oceans*, 114.
- PERILLO, M. M., BEST, J. L. & GARCIA, M. H. 2014a. A new phase diagram for combined-flow bedforms. *Journal of Sedimentary Research*, 84, 301-313.
- PERILLO, M. M., BEST, J. L., YOKOKAWA, M., SEKIGUCHI, T., TAKAGAWA, T. & GARCIA, M. H. 2014b. A unified model for bedform development and equilibrium under unidirectional, oscillatory and combined-flows. *Sedimentology*, 61, 2063-2085.
- PRECHT, E. & HUETTEL, M. 2003. Advective pore - water exchange driven by surface gravity waves and its ecological implications. *Limnology and Oceanography*, 48, 1674-1684.
- RALSTON, D. K., WARNER, J. C., GEYER, W. R. & WALL, G. R. 2013. Sediment transport due to extreme events: The Hudson River estuary after tropical storms Irene and Lee. *Geophysical Research Letters*, 40, 5451-5455.
- RUBIN, D. M. & CARTER, C. L. 2005. *Bedforms 4.0: MATLAB code for simulating bedforms and cross-bedding*, US Geological Survey.
- SCHERER, M., MELO, F. & MARDER, M. 1999. Sand ripples in an oscillating annular sand-water cell. *Physics of Fluids*, 11, 58-67.

- SNELGROVE, P. & BUTMAN, C. 1995. Animal-sediment relationships revisited: cause versus effect. *Oceanographic Literature Review*, 8, 668.
- SOULSBY, R. 1997. *Dynamics of marine sands: a manual for practical applications*, Thomas Telford.
- SOULSBY, R. & CLARKE, S. 2005. Bed shear-stress under combined waves and currents on smooth and rough beds (TR 137).
- SOUTHARD, J. B. 1991. Experimental determination of bed-form stability. *Annual Review of Earth and Planetary Sciences*, 19, 423-455.
- STAUDT, F., MULLARNEY, J. C., PILDITCH, C. A. & HUHN, K. 2017. The role of grain-size ratio in the mobility of mixed granular beds. *Geomorphology*, 278, 314-328.
- STEGNER, A. & WESFREID, J. E. 1999. Dynamical evolution of sand ripples under water. *Physical review E*, 60, R3487.
- TANAKA, H. & DANG, V.T. 1996. Geometry of sand ripples due to combined wave-current flows. *Journal of waterway, port, coastal, and ocean engineering*, 122, 298-3000.
- VAN DER MARK, C., BLOM, A. & HULSCHER, S. 2008. Quantification of variability in bedform geometry. *Journal of Geophysical Research: Earth Surface*, 113.
- VAN DER WERF, J. J., MAGAR, V., MALARKEY, J., GUIZIEN, K. & O'DONOGHUE, T. 2008. 2DV modelling of sediment transport processes over full-scale ripples in regular asymmetric oscillatory flow. *Continental Shelf Research*, 28, 1040-1056.
- VAN RIJN, L. C. 2007. Unified view of sediment transport by currents and waves. I: Initiation of motion, bed roughness, and bed-load transport. *Journal of Hydraulic engineering*, 133, 649-667.
- WENGROVE, M., FOSTER, D., LIPPMANN, T., DE SCHIPPER, M. & CALANTONI, J. 2018. Observations of Time-Dependent Bedform Transformation in Combined Wave-Current Flows. *Journal of Geophysical Research: Oceans*, 123, 7581-7598.
- WOODRUFF, J. D., IRISH, J. L. & CAMARGO, S. J. 2013. Coastal flooding by tropical cyclones and sea-level rise. *Nature*, 504, 44-52.
- WU, X., BAAS, J. H., PARSONS, D. R., EGGENHUISEN, J., AMOUDRY, L., CARTIGNY, M., MCLELLAND, S., MOUAZÉ, D. & RUESSINK, G. 2018. Wave Ripple Development on Mixed Clay-Sand Substrates: Effects of Clay Winnowing and Armoring. *Journal of Geophysical Research: Earth Surface*, 123, 2784-2801.